

J. Sznitman · R. Sutter · D. Altorfer · M. Stampanoni · T. Rösgen ·  
J. C. Schittny

## Visualization of respiratory flows from 3D reconstructed alveolar airspaces using X-ray tomographic microscopy

Received: 10 October 2009 / Accepted: 12 May 2010 / Published online: 20 June 2010  
© The Visualization Society of Japan 2010

**Abstract** A deeper knowledge of the three-dimensional (3D) structure of the pulmonary acinus has direct applications in studies on acinar fluid dynamics and aerosol kinematics. To date, however, acinar flow simulations have been often based on geometrical models inspired by morphometrical studies; limitations in the spatial resolution of lung imaging techniques have prevented the simulation of acinar flows using 3D reconstructions of such small structures. In the present study, we use high-resolution, synchrotron radiation-based X-ray tomographic microscopy (SRXTM) images of the pulmonary acinus of a mouse to reconstruct 3D alveolar airspaces and conduct computational fluid dynamic (CFD) simulations mimicking rhythmic breathing motion. Respiratory airflows and Lagrangian (massless) particle tracking are visualized in two examples of acinar geometries with varying size and complexity, representative of terminal sacculi including their alveoli. The present CFD simulations open the path towards future acinar flow and aerosol deposition studies in complete and anatomically realistic multi-generation acinar trees using reconstructed 3D SRXTM geometries.

**Keywords** Synchrotron radiation X-ray tomographic microscopy (SRXTM) · Computational fluid dynamics (CFD) · Pulmonary acinus · Alveolar flow

### 1 Introduction

Relatively few quantitative data describe the three-dimensional (3D) structure of the pulmonary acinus. With growing numbers of epidemiological studies suggesting that air-borne particles convey adverse health effects (Brunekreef and Holgate 2002), the lack of 3D information on the acinus becomes more critical if we hope to understand and to predict the deposition of inhaled substances. Traditionally, acinar morphology has been studied using measurements of mammalian-lung casts (Haefeli-Bleuer and Weibel 1988)

---

J. Sznitman (✉)

Department of Mechanical and Aerospace Engineering, Princeton University, Princeton, NJ 08544, USA  
E-mail: sznitman@princeton.edu

M. Stampanoni

Swiss Light Source Project, Paul Scherrer Institute, 5232 Villigen, Switzerland

M. Stampanoni

Institute of Biomedical Engineering, ETH Zurich, 8092 Zurich, Switzerland

R. Sutter · D. Altorfer · T. Rösgen

Institute of Fluid Dynamics, ETH Zurich, 8092 Zurich, Switzerland

J. C. Schittny

Institute of Anatomy, University of Bern, 3010 Bern, Switzerland

or described using serial histological section techniques (Hansen and Ampaya 1975; Hansen et al. 1975). 3D reconstruction of alveoli was first brought from serial histological sections (Mercer and Crapo 1987), although reconstruction was restricted to few alveoli due to technical limitations. With modern imaging techniques including computed tomography (CT), 3D lung models have become more widespread (Brown et al. 1991; McNamara et al. 1992; Kitaoka et al. 2000). This progress has led to the reconstruction of bronchial trees and small airways (Aykac and Hoffman 2003; Sauret et al. 2002; Sera et al. 2003). However, 3D reconstruction of the acinar region has remained largely prohibited due to limitations in spatial resolution using  $\mu$ CT techniques.

This limitation has been overcome with the development of synchrotron radiation-based X-ray tomographic microscopy (SRXTM). This technique remains exclusive due to the few facilities available worldwide. Synchrotrons constitute cyclic particle accelerators in which magnetic and electric fields are synchronized with the traveling particle beam, and are mostly used for producing high-intensity X-ray beams. With this technique, high spatial resolution imaging and 3D reconstruction of small airways and alveoli have been obtained (Schittny et al. 2008; Tsuda et al. 2008).

The pursuit towards anatomically realistic 3D acinar structures has direct applications in studies on fluid dynamics and particle deposition in the lungs. Due to limited accessibility of this region and the lack of 3D imaging data, airflows have remained generally difficult to assess. Hence, considerable progress has been brought with numerical studies, offering insight on acinar deposition of inhaled fine particles. Traditionally, simulations have made use of alveolated geometries inspired from morphometry (Haefeli-Bleuer and Weibel 1988). Acinar airways have been modeled using cylindrical ducts mounted with spherical cavities, in 2D (Darquenne 2001; Henry et al. 2002; Tsuda et al. 1995) and 3D simulations (Haber et al. 2003; Sznitman et al. 2007). More recently, space-filling acinar geometries have been introduced (Sznitman et al. 2009).

In the present study, high-resolution SRXTM of the pulmonary mouse acinus is used to reconstruct anatomically realistic 3D geometries of terminal alveolar airspaces. Computational fluid dynamic (CFD) simulations of airflows and massless particle trajectories are illustrated in two representative saccular geometries of varying size and complexity. Such geometries were chosen to investigate whether differences in saccular size and topology may influence the basic acinar flow structures operating at low Reynolds number under self-similar breathing conditions. We discuss some current limitations pertinent to the 3D reconstruction with an outlook on future CFD studies in anatomically realistic reconstructed multi-generation acinar networks.

## 2 Methods

In the present study, lungs of 10-day-old 129/SV mice were prepared as described previously (Haas et al. 2003; Luyet et al. 2002). Imaged samples were prepared according to recent protocols, and may be found in (Schittny et al. 2008; Tsuda et al. 2008). Airspace was filled with 2.5% glutaraldehyde in 0.03 M potassium-phosphate buffer (pH 7.4, 370 mOsm) at a constant pressure of 20 cm water column. At this pressure, the lung is fixed close to its total lung capacity (TLC). To prevent a recoiling of the lung, the pressure was maintained during fixation ( $>2$  h). Samples were postfixed in 0.1 M sodium cacodylate (pH 7.4, 340 mOsm), containing 1% OsO<sub>4</sub>, and stained en bloc with 0.5% uranyl acetate in 0.05 M maleate buffer. After dehydration in a graded series of ethanol, the samples were embedded in Epon 812. Epon is chosen as embedding material, because shrinking of the tissue is very small (5% or less). Handling of the animals before and during the experiments, as well as the experiments themselves, were approved and supervised by the Swiss Agency for the Environment, Forests and Landscape and the Veterinary Service of the Canton of Bern.

Samples were scanned at 12.398 keV according to (Stampanoni et al. 2002). After penetration of the sample, X-rays were converted into visible light by a thin Ce-doped YAG scintillator screen. Projection images were magnified by a light microscope and digitized by a CCD camera (Stampanoni et al. 2002). Optical magnification was set to 10 $\times$  and on-chip 2  $\times$  2 binning was selected to improve the signal-to-noise ratio, resulting in isotropic voxels of 1.43  $\mu\text{m}^3$ . 1,001 projections were acquired along with dark and periodic flat field images for each sample. Before reconstruction into a 3D-stack of SRXTM-images, the data were post-processed and rearranged into flat field corrected sinograms. Examples of SRXTM images are shown in Fig. 1.

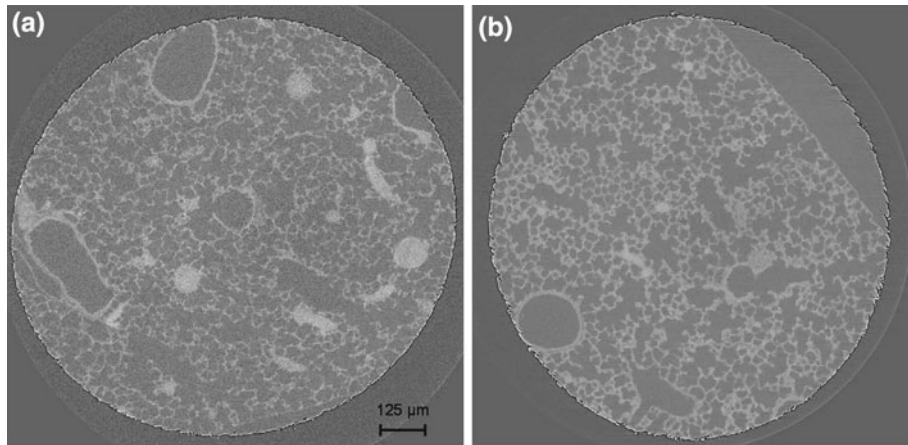


**Fig. 1** Two representative SRXTM image slices with spatial planar resolution of  $1.4 \mu\text{m} \times 1.4 \mu\text{m}$  obtained from the pulmonary acinus of a 10-day-old mouse. Cross-sections of small airways are visible (e.g. top of **a** and bottom left of **b**), while the visceral pleura (surface of the lung) is visible along the upper right region of **b**

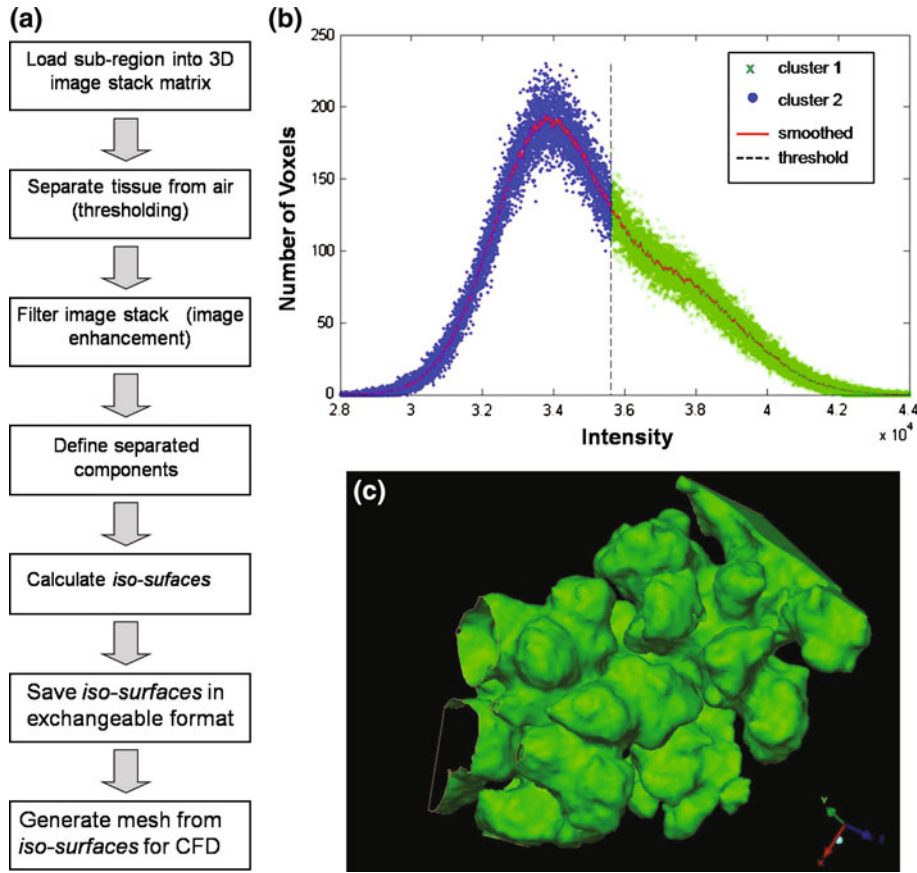
## 2.1 3D reconstruction

Image segmentation and 3D surface rendering are obtained from an in-house developed script using Matlab. The image processing steps are depicted schematically in Fig. 2a. 3D reconstruction is restricted here to sub-regions extracted from SRXTM image stacks; respiratory simulations in complete multi-generation acinar trees lie beyond current feasibility. SRXTM data ( $\sim 100 \times 100 \text{ pixels} \times 100 \text{ slices}$ ) are extracted near outer edges of the lung parenchyma (Fig. 1b). Such locations coincide with distal regions of the acinus, where terminal alveolar sacs are thought to be found.

For CFD simulations, airspaces rather than alveolar wall septa are reconstructed. First, separation of lung tissue from air is obtained using a thresholding technique applied to intensity values of the voxels. High intensity values correspond to lung tissue; lower ones are attributed to air. Since there are only two different materials present, namely air and lung tissue, the problem may be reduced to finding a single threshold value over the entire image stack. Looking at a characteristic intensity histogram of an SRXTM image stack (Fig. 2b), it becomes clear that the intensity distribution is not purely bimodal. Rather, air and tissue exhibit imperfect contrast and their intensity ranges overlap significantly and blend into one another. Therefore, setting a single threshold value will always amount to a tradeoff between having too thick alveolar walls and correspondingly creating a loss of airspace, versus setting a threshold value too high and risking to create artifacts such as holes in the alveolar walls (Tsuda et al. 2008).

To optimize separation of lung tissue from air, a balance is chosen between direct visual thresholding and an iterative  $K$ -means clustering algorithm. This latter algorithm minimizes the sum of point-to-centroid distances, summed over  $K$  clusters ( $K = 2$ ). The mean of the resulting two cluster centers is used as an initial threshold value (Fig. 2b). Further corrections, if needed, are implemented by visual thresholding. The presence of intrinsic noise in raw SRXTM data can potentially jeopardize successful 3D reconstruction. To obtain meaningful geometries and avoid artifact generation inside airspaces (scatter voxels due to noise can be wrongly attributed with tissue because of their relatively high intensity values), noise elimination is sought through digital filters. Accordingly, a median filter with adjustable  $N \times N$  window size is applied to each image slice. The advantages of this filter are its simplicity and reasonable edge-preservation. Median filtering yields satisfactory results, although small drawbacks in edge-preserving filtering techniques, such as edge smoothing, are intrinsic.

Next, clusters of airspaces are constructed. Here, an iterative algorithm assigns one component to each voxel over the image stack: (1) for each voxel attributed with air, the neighboring, previously visited voxels are checked for voxels also attributed with air; (2) if an air-voxel is found in this neighborhood, the current voxel is assigned the same component number as the neighboring air-voxel, thus added to the component corresponding to this number; (3) alternatively, if no such air-voxel is found in the previously visited neighborhood, the current voxel is assigned with the next free component number. Finally, iso-surfaces are constructed to generate 3D geometries. For a 3D matrix representing an image stack, a surface within the volume with the same value at each vertex is calculated (iso-value). Optionally, the 3D matrix is first



**Fig. 2** **a** Image processing steps for 3D reconstruction of acinar airspaces. **b** Histogram of intensity values of a sample image stack from SRXTM data for a 10-day-old mouse. The threshold value separating air (cluster 1) from lung tissue (cluster 2) is found from the mean of the resulting centers obtained from a 2-means clustering algorithm. **c** Reconstructed 3D alveolar airspaces. Typical alveolar diameters range between 15 and 40  $\mu\text{m}$

smoothed to reduce abrupt changes between neighboring polygon normals of the calculated polygonal iso-surfaces. On outer borders, where iso-surfaces are cut by the bounding box spanning the size of the stack, isocaps are defined to form closed bodies together with the iso-surfaces. The mesh formed by calculated iso-surfaces is stored in an exchangeable format (vrml-file) compatible with the flow solver (Ansys CFX, ANSYS, Inc. Canonsburg, PA, USA).

## 2.2 Numerical methods

Numerical schemes are described in detail in recent studies using geometrical acinar models (Sznitman et al. 2007, 2009). Briefly, to accommodate for self-similar breathing (Ardila et al. 1974; Gil et al. 1979), acinar geometries are designed to expand/contract in a sinusoidal manner, with breathing period  $T$  ( $f = 1/T$ ). The specific volume excursion is given by  $C = (V_{\max} - V_{\min})/V_{\min}$ , where  $V_{\min}$  and  $V_{\max}$  are, respectively, the minimum/maximum acinar volumes. The length scale expansion factor is given by  $\beta = (C + 1)^{1/3} - 1$ . Breathing conditions mimic tidal breathing of a mouse (Bonara et al. 2004; Pokorski et al. 2005), with  $T = 0.4$  s,  $C \approx 19\%$ , and  $\beta \approx 6\%$ . Although acinar geometries represent volumes near total lung capacity (TLC), airflow in terminal airspaces is governed by basic wall motion (Sznitman et al. 2007; Tsuda et al. 1995); the magnitude of the fluid volumes displaced during simulation do not alter appreciably the structure of the resulting flow patterns. Time-dependent flows are obtained from solving numerically the incompressible Navier-Stokes equations on a moving grid, using a commercial finite-volume-based program with fully implicit marching techniques (CFX-11, Ansys Inc.). Once the velocity field ( $\underline{u}(x, t)$ ) is solved, Lagrangian trajectories of fluid (massless) particles ( $x(t)$ ) are integrated using a forward Euler integration scheme.

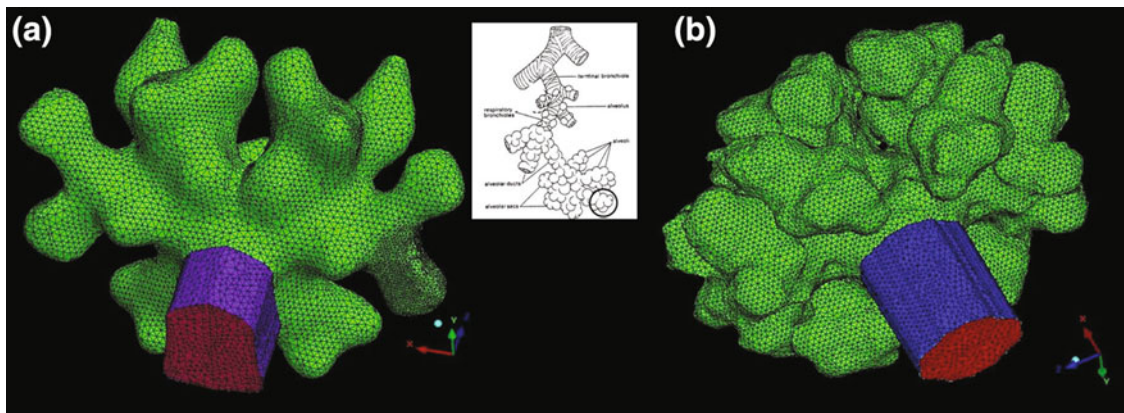


**Fig. 3** Meshes for the reconstructed 3D alveolar sacs of **a** geometry I and **b** II. Geometries are characterized by the existence of symmetry planes and the presence of a short entrance duct feeding the alveolar space (shown in distinct color). Inset Schematic representation of the acinus with the location of an alveolar sac circled (modified from Haber and Tsuda 1998)

### 3 Results

An example of a reconstructed cluster of alveoli is shown in Fig. 2c. Resulting geometries present qualitatively similar features to 3D surfaces obtained using commercial imaging software (Mund et al. 2008; Schittny et al. 2008), although such studies focused rather on reconstructing acinar lung tissue surfaces rather than airspaces. For CFD, a bounded flow domain must be constructed. This is shown in Fig. 3, with two distinct saccular geometries, we are interested in understanding whether the specific alveolar sacs geometries may lead or not to unique flow characteristics at low Reynolds number, for self-similar breathing conditions. For each alveolar sac geometry, an unstructured hybrid mesh is generated consisting of prisms and tetrahedron volume elements. Geometry I is made of approximately 280,000 volume elements, corresponding to an initial volume of  $\sim 0.8 \times 10^{-3} \mu\text{L}$  ( $t = 0$ ). Similarly, geometry II is made of 600,000 volume elements corresponding to an initial volume of  $\sim 2.7 \times 10^{-3} \mu\text{L}$ .

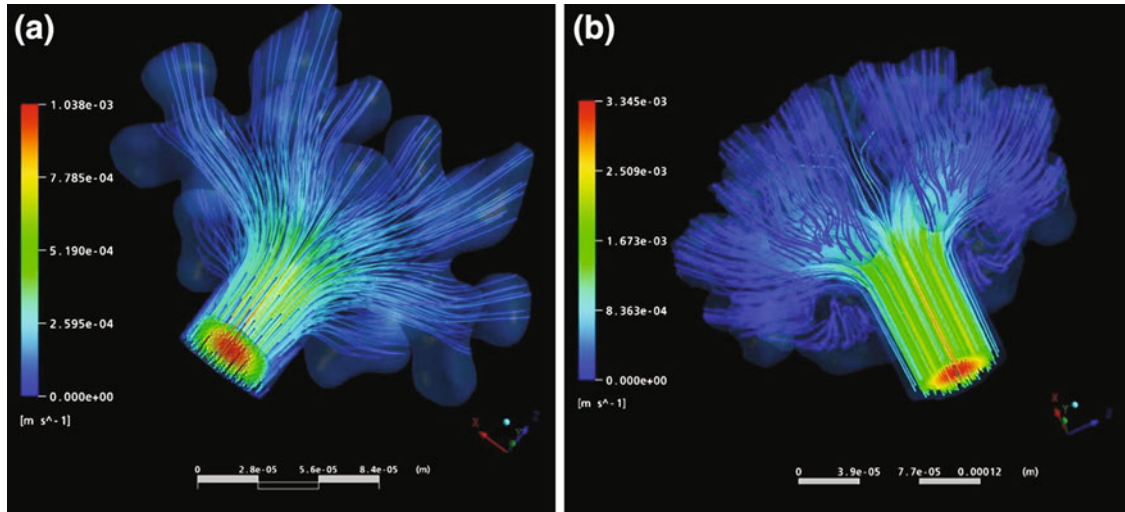
Initially, both geometries exhibit artificial planes near the domain boundaries. These planes result from the 3D reconstruction steps: (1) the separation of air volumes and (2) the presence of the exterior bounding box. To resolve this problem, alveolar geometries are mirrored about such planes and connected along the mirrored surfaces to obtain bounded domains. Next, a short duct of is added to feed airflow into each reconstructed airspace (geometry I and II). Each duct was designed to guarantee that the effects of the velocity profile on the alveolar flow are negligible (Fig. 3). For low Reynolds number flows in ducts ( $Re \ll 1$ ), it takes an entrance length ( $L_e$ ) of approximately 0.6 diameters to change from a uniform velocity profile to a parabolic profile (Shah and London 1978). Hence, the artificial ducts added at the entrance of the alveolar sacs are designed with  $L/D \gg 1$ , where  $L$  is the entrance duct length. Here, the original dimensions of the alveolar airspace opening are  $D \approx 55$  and  $60 \mu\text{m}$ , respectively, for geometry I and II. This is shown in Fig. 3, where geometry II displays a longer and wider duct relative to geometry I.

Figure 4 illustrates resulting flow streamlines at peak inspiration ( $t = 0.1 \text{ s}$ ). In both terminal sacculi, flow topologies are similar despite size and complexity. Streamlines are radial, with a mean Reynolds number ( $\overline{Re} = \overline{UD}/v$ , where  $v$  is the air viscosity) at the duct inlet of  $\overline{Re} \sim 0.001$  and  $\sim 0.0035$ , respectively, for geometry I and II. Note that during simulations, the entire structure (i.e. alveolar sac + entrance duct) is subjected to self-similar breathing motion so as to assure matching moving wall conditions and avoid any kinematic singularity in wall motions. We find that flow topology does not change appreciably throughout the breathing period, emphasizing that basic flow characteristics are insensitive to global  $Re$  effects (Tsuda et al. 1995). This follows from low values of the dimensionless frequency parameter, i.e. the Womersley number,  $\overline{Wo} = \overline{D}(f/v)^{1/2} \sim 0.02$ , underlining that flow in terminal sacculi is quasi-steady.

Particle trajectories are computed over cumulative breathing cycles (Figs. 5, 6). Two arbitrary yet representative injection locations are illustrated here: location A is situated near the entrance of an alveolus far from the inlet; location B is chosen closer to the entrance duct. In geometry I (Fig. 5), trajectories at location A exhibit nearly reversible paths, with a negligible drift of  $\sim 1 \mu\text{m}$  over the period  $t = 0$  to  $5T = 2 \text{ s}$ . At location B, the total drift observed is increased over the same period to  $\sim 8 \mu\text{m}$ . At the same time, we note that particles at location B have a peak velocity magnitude of approximately  $7.1 \mu\text{m/s}$ , while

those at location *A* peak near  $5.8 \mu\text{m}/\text{s}$ . Within the limits of our results, we speculate that the differences observed between trajectories at locations *A* and *B* may be attributed in part to a small yet significant increase in velocities observed near the entrance duct compared to within the bulk of the airspace. In general, particle trajectories observed here (Figs. 5, 6) compare qualitatively well with those seen for drifting massless particles inside alveolar cavities under similar flow conditions (Tsuda et al. 1995).

In geometry II, trajectories of passive tracers are followed over 4 breathing periods at location *A* and *B*, respectively. Since the initial volume of the acinar sac is approximately 3.4 times larger than in geometry I, airflow velocities observed within the bulk of the airspace are increased relative to those seen in the former geometry (Fig. 4); this is a direct consequence of mass conservation. In addition, velocity magnitudes are largest near the duct entrance and rapidly decrease as one travels deeper into the bulk airspace. Hence, particles at location *B* exhibit longer trajectory paths relative to those seen at location *A* (Fig. 6); the overall drift is also relatively larger at location *B*. Overall similar trends are noted in the general particle transport



**Fig. 4** Instantaneous alveolar streamlines with velocity field magnitude in three-dimensional space, obtained at peak inspiration ( $t = 0.1$  s) in alveolar sac geometries (a) I and (b) II. Color bars denote velocity magnitude in (m/s)

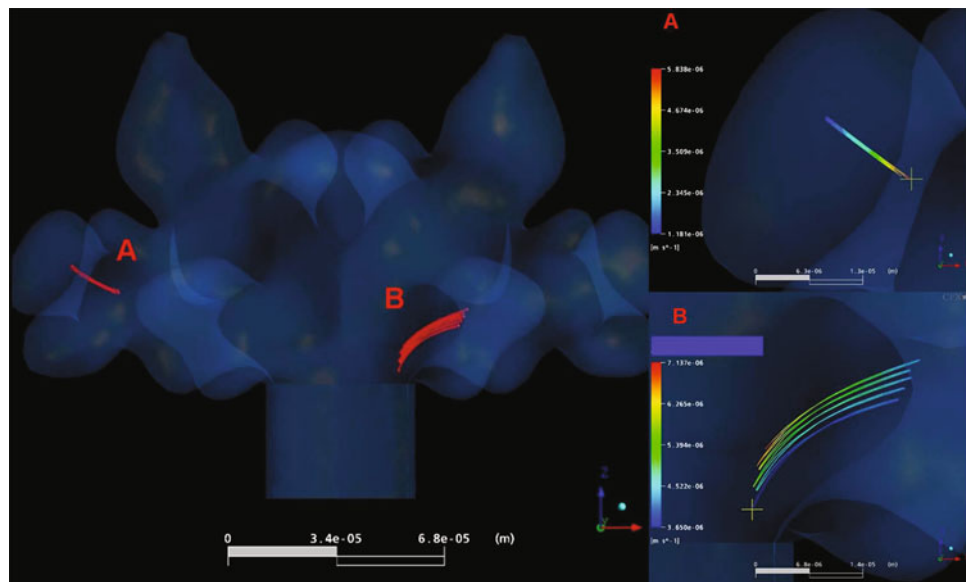


**Fig. 5** Massless particle trajectories in geometry I over 5 breathing cycles. Two injection points are illustrated: site *A* is located near the entrance of an alveolus and site *B* is closer to the entrance duct. Insets correspond to close-ups of particle trajectory originating from points *A* and *B*. Color bar illustrates velocity magnitude (m/s) of particles along pathline

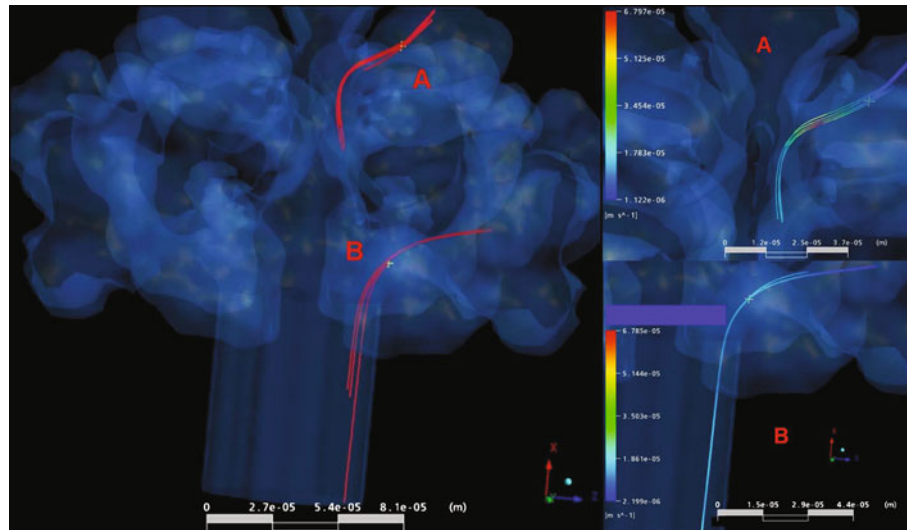


**Fig. 6** Massless particle trajectories in geometry II over 4 breathing cycles. Two injection points are illustrated: site A is located near the entrance of an alveolus and site B is closer to the entrance duct. Insets correspond to close-ups of particle trajectory originating from points A and B. Color bar illustrates velocity magnitude (m/s) of particles along pathline

behaviors seen between geometry I and II. However, a detailed investigation on the transport factors leading to particle drift lies beyond the scope of the present study; additional breathing protocols different from sole tidal breathing in a mouse must be studied. In the present article we have limited our discussion on the general feasibility of conducting respiratory flow simulations within reconstructed alveolar airspaces. Further discussion on the convective mechanisms governing particle transport and drift during cyclic breathing motion within acinar geometries may be found in our recent study (Sznitman et al. 2009).

We briefly discuss the potential influence of integration time steps and pathline curvature on obtaining reliable particle transport. First, transient solutions at time step  $\Delta t$  are ensured such that the Courant number ( $Co = \Delta t \cdot u / \Delta x$ ) relating the ratio of  $\Delta t$  to the cell residence time ( $\Delta x / u$ ), where  $\Delta x$  is the cell element size, yield  $Co < 0.1$  (Ferziger and Peric 2001). To guarantee this condition, we implemented  $\Delta t = 0.05 \cdot T = 0.02$  s. At low  $Re$  number, the use of a first-order forward Euler integration scheme is satisfactory: convection is weak and particle inertial effects are nonexistent for passive tracers. Hence, particle motion may be approximated as resulting from purely linear translations. This is valid if small integration time steps ( $\Delta t$ ) are implemented (1) for computational convergence (as described above) and simultaneously (2) to guarantee small displacements during the integration scheme. Such incremental displacements can follow adequately curvilinear flow streamlines (Darmofal and Haimes 1996), which exist in our acinar geometries. In particular, following the criterion  $\Delta t_{\max} = \eta l / |u|$  (Darmofal and Haimes 1996), where  $l$  is the local cell size,  $\eta$  is the allowable cell size which a particle may travel in a single time step, and  $|u|$  is the magnitude of the local velocity, we find  $\Delta t_{\max} \approx O(2 \times 10^{-2}$  s) when choosing  $\eta = 1$  for example (a particle can travel up to a distance  $l$  over a time step  $\Delta t$ ). Following this criterion,  $\Delta t = 0.02$  s is comparable to  $\Delta t_{\max}$ .

#### 4 Discussion and conclusion

Reconstructed alveoli (Fig. 2c) do not form tightly bounded space-filling structures (Fung 1988). This follows since reconstructed geometries represent alveolar airspaces only, while alveolar septum is disregarded. Hence, alveolar airspaces cannot lie in direct contact with their neighbors due to the finite thickness of the alveolar septum. The relatively large separations qualitatively seen between individual alveoli may also arise due to other factors. (1) During lung development, the alveolar septa of a mouse are relatively thicker at 10 days old than in adult (Burri et al. 1974; Roth-Kleiner et al. 2005), yielding a relative increase in the space separating each alveolus. (2) The threshold value for segmentation may slightly increase the alveolar wall thickness to avoid creating artificial holes in the alveolar septum (Tsuda et al. 2008).

One must also consider the possibility of artificial changes in tissue dimensions occurring with preparation. The influence of fixing, dehydrating, and embedding agents may perhaps introduce changes in dimensions of lung tissue structures from the fresh to the processed specimen. Shrinking of the specimen

may be estimated on the order of ~5 % (Weibel and Knight 1964). This value remains negligible and the final shape of the reconstructed airspaces is not substantially influenced by the specimen preparation.

Flows in terminal sacculi are characterized by radial flow fields with quasi-reversible particle trajectories (Figs. 4–6). For chaotic particle kinematics to arise, chaotic flow behavior is anticipated (Tsuda et al. 1995). However, chaotic acinar flows are known to result from the presence of recirculation regions characterized with stagnation saddle points. Physically, recirculation must result from relatively strong ductal shear flows passing over an alveolar opening coupled with radial alveolar flows due to expansion/contraction motion (Sznitman et al. 2007; Tsuda et al. 1995). Physiologically, strong ductal flows exist in proximal regions of the acinar tree; acinar ducts feed the entire network of distal airways and alveoli (Sznitman et al. 2009). In contrast, airflows in terminal sacculi are dominated by low *Re* number radial flows, induced solely from wall motion operating at low *Wo* number. This is seen in the acinar flows of geometry I and II (Fig. 4); basic flow structures are overwhelmingly insensitive to the specific size and complexity of the saccular topology. Note that alveoli in terminal sacs do not cover ducts. Rather, they form a closed end chamber. Hence, chaotic flow behavior resulting from ductal shear flows is not seen in the present 3D reconstructed geometries.

SRXTM imaging offers reliable imaging for CFD applications, yielding possibly even lower spatial resolutions (Stampanoni et al. 2002). Yet, the extraction of sub-regions from SRXTM data coupled with low intensity contrast images have limited 3D reconstruction to terminal sacculi only. The potential use of SRXTM data from patient-specific lungs holds promise for future acinar deposition studies. Also, intricate aerosol kinematics spanning entire acinar space-filling networks before deposition may be examined (Sznitman et al. 2009). Finally, the prospective use of multi-generation acinar trees opens the path towards deposition studies where streamline crossing takes place (e.g. diffusion). This latter issue is of particular relevance as the interest in the fate of inhaled ultrafine particles (<100 nm) continues to increase (Muhrfeld et al. 2008).

## References

- Ardila R, Horie T, Hildebrandt J (1974) Macroscopic isotropy of lung expansion. *J Appl Physiol* 20:105–115
- Aykac D, Hoffman EA (2003) Segmentation and analysis of the human airway tree from three-dimensional X-ray CT images. *IEEE Trans Med Imaging* 22:940–950
- Bonara M, Bernaudin JF, Guernier C, Brahimi-Horn MC (2004) Ventilatory responses to hypercapnia and hypoxia in conscious cystic fibrosis knockout mice Cftr<sup>−/−</sup>. *Pediatr Res* 55:738–746
- Brown RH, Herold CJ et al (1991) In vivo measurements of airway reactivity using high resolution computed tomography. *Am Rev Respir Dis* 144:208–212
- Brunekeef B, Holgate ST (2002) Air pollution and health. *Lancet* 360:1233–1242
- Burri PH, Dbaly J, Weibel ER (1974) The postnatal growth of the rat lung. I. Morphometry. *Anat Rec* 178:711–730
- Darmofal DL, Haimes R (1996) An analysis of 3D particle path integration algorithms. *J Comp Phys* 123:182–195
- Darquenne C (2001) A realistic two-dimensional model of aerosol transport and deposition in the alveolar zone of the human lung. *J Aerosol Sci* 32:1161–1174
- Ferziger JH, Peric M (2001) Computational methods for fluid dynamics, 3rd edn. Springer, Berlin
- Fung YC (1988) A model of the lung structure and its validation. *J Appl Physiol* 64:2132–2141
- Gil J, Bachofen H, Gehr P, Weibel ER (1979) Alveolar volume-surface area relation in air- and saline-filled lungs fixed by vascular perfusion. *J Appl Physiol* 45:990–1001
- Haas CS, Amann K, Schittny JC et al (2003) Glomerular and renal vascular structural changes in alpha 8 integrin-deficient mice. *J Am Soc Nephrol* 14:2288–2296
- Haber S, Tsuda A (1998) The effect of flow generated by a rhythmically expanding pulmonary acinus on aerosol dynamics. *J Aerosol Sci* 29:309–322
- Haber S, Yitzhak D, Tsuda A (2003) Gravitational deposition in a rhythmically expanding and contracting alveolus. *J Appl Physiol* 95:657–671
- Haefeli-Bleuer B, Weibel ER (1988) Morphometry of the human pulmonary acinus. *Anat Rec* 220:401–414
- Hansen JE, Ampaya EP (1975) Human air space shape, sizes, areas and volumes. *J Appl Physiol* 38:990–995
- Hansen JE, Ampaya EP, Bryant GH, Navin JJ (1975) Branching pattern of airways and air spaces of a single human terminal bronchiole. *J Appl Physiol* 38:983–989
- Henry FS, Butler JP, Tsuda A (2002) Kinematically irreversible acinar flow: a departure from classical dispersive aerosol transport theories. *J Appl Physiol* 92:835–845
- Kitaoka H, Tamura S, Takaki R (2000) A three-dimensional model of the human pulmonary acinus. *J Appl Physiol* 88:2260–2268
- Luyet C, Burri PH, Schittny JC (2002) Suppression of cell proliferation and programmed cell death by dexamethasone during postnatal lung development. *Am J Physiol Lung Cell Mol Physiol* 282:L477–L483
- McNamara AE, Muller NL, Okazawa M et al (1992) Airway narrowing in excised canine lungs measured by high-resolution computed tomography. *J Appl Physiol* 73:307–316
- Mercer RR, Crapo JD (1987) Three-dimensional reconstruction of the rat acinus. *J Appl Physiol* 63:785–794

- Muhlfeld C, Rothen-Ruthishauser B, Blank F et al (2008) Interactions of nanoparticles with pulmonary structures and cellular responses. *Am J Physiol Lung Cell Mol Physiol* 294:L817–L829
- Mund SI, Stampanoni M, Schittny JC (2008) Developmental alveolarization of the mouse lung. *Dev Dyn* 237:2108–2116
- Pokorski M, Izumizaki M, Homma I (2005) Transient O<sub>2</sub>-dependent effect of CO<sub>2</sub> on ventilation in the anesthetized mouse. *J Physiol Pharmacol* 56:447–454
- Roth-Kleiner M, Berger TM, Tarek MR et al (2005) Neonatal Dexamethasone induces premature microvascular maturation by focal fusion of alveolar capillaries. *Dev Dyn* 233:1261–1271
- Sauret V, Halson PM, Brown IW et al (2002) Study of the three-dimensional geometry of the central conducting airways in man using computed tomographic (CT) images. *J Anat* 200:123–134
- Schittny JC, Mund SI, Stampanoni M (2008) Evidence and structural mechanism for late lung alveolarization. *Am J Physiol Lung Cell Mol Physiol* 294:L246–L254
- Sera T, Fujioka H, Yokota H et al (2003) Three-dimensional visualization and morphometry of small airways from microfocal X-ray computed tomography. *J Biomech* 36:1587–1594
- Shah RK, London AL (1978) Laminar flow forced convection in ducts. Academic, New York
- Stampanoni M, Borchet G, Wyss P et al (2002) High resolution X-ray detector for synchrotron based microtomography. *Nucl Instr Meth A* 491:291–301
- Sznitman J, Heimsch F, Heimsch T et al (2007) Three-dimensional convective alveolar flow induced by rhythmic breathing motion of the pulmonary acinus. *ASME J Biomed Eng* 129:658–665
- Sznitman J, Heimsch T, Wildhaber JH et al (2009) Respiratory flow phenomena and gravitational sedimentation in a three-dimensional space-filling model of the pulmonary acinar tree. *ASME J Biomed Eng* 131:031010
- Tsuda A, Filipovic N, Haberthuer D et al (2008) Finite element 3D reconstruction of the pulmonary acinus imaged by synchrotron X-ray tomography. *J Appl Physiol* 105:964–976
- Tsuda A, Henry FS, Butler JP (1995) Chaotic mixing of alveolated duct flow in rhythmically expanding pulmonary acinus. *J Appl Physiol* 79:1055–1063
- Weibel ER, Knight BW (1964) A morphometric study on the thickness of the pulmonary air–blood barrier. *J Cell Biol* 21:367–384